J. Fluid Mech. (2023), *vol*. 966, A23, doi:10.1017/jfm.2023.436

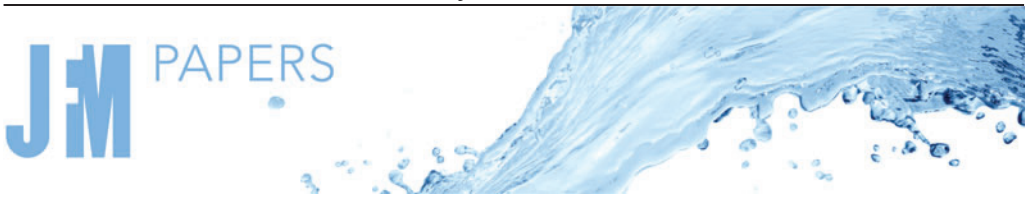

Particle orbiting constrained by elastic filament as a model cilium for fluid pumping

Shiyuan Hu[1],† **and Fanlong Meng**[1,2,3],†

[1]CAS Key Laboratory of Theoretical Physics, Institute of Theoretical Physics, Chinese Academy of Sciences, Beijing 100190, PR China

[2]School of Physical Sciences, University of Chinese Academy of Sciences, 19A Yuquan Road, Beijing 100049, PR China

[3]Center for Theoretical Interdisciplinary Sciences, Wenzhou Institute, University of Chinese Academy of Sciences, Wenzhou 325001, PR China

(Received 24 December 2022; revised 18 March 2023; accepted 24 May 2023)

Many microorganisms use cilia to propel themselves in low Reynolds number (*Re*) environments. In this work, we study the dynamics of a composite cilium consisting of an elastic filament and a spherical particle attached at the filament tip driven by an external time-periodic force acting on the particle. The elastic filament is modelled numerically using a slender body theory with hydrodynamic interactions. When tilted at a large angle from the normal direction of the wall, the filament buckles, and the induced velocity field by the cilium shows a large net flux. By varying the tilt angle or the force amplitude, the particle trajectory and the net flux display abrupt changes along with a reversal of the buckling direction. We further demonstrate through a segmental model that the abrupt changes arise from the deviation of the cilium orientation at the start of the recovery stroke from the natural orientation. Our results suggest a simple approach to engineering particle motions and designing artificial cilia for fluid pumping in low *Re* environments.

Key words: slender-body theory, Stokesian dynamics, microscale transport

1. Introduction

Cilia are thin hair-like cellular protrusions that serve a variety of fundamental roles in many eukaryotes. The internal structure has a characteristic '9+2' arrangement of microtubules. Driven by the distributed sliding forces acting on neighbouring microtubules by molecular motors, cilia beat asymmetrically with a distinct power and recovery stroke to break the time-reversal symmetry and generate net propulsion at low Reynolds number (*Re*) (Blake & Sleigh 1974; Purcell 1977). One hypothesis for the spontaneous beating is based on dynamic instabilities developed when the motor activity exceeds a threshold

† Email addresses for correspondence: shiyuan.hu@itp.ac.cn, fanlong.meng@itp.ac.cn

(Camalet, Julicher & Prost 1999; Bayly & Dutcher 2016; Oriola, Gadêlha & Casademunt 2017; Ling, Guo & Kanso 2018). Cilia can also beat collectively in dense arrays to form metachronal waves via hydrodynamic interactions (Meng *et al.* 2021; Chakrabarti, Fürthauer & Shelley 2022; Kanale *et al.* 2022), and such collective motions play crucial roles in the locomotion and material transport of many microorganisms and tissues (Lauga & Powers 2009; Faubel *et al.* 2016; Juan *et al.* 2020).

Inspired by natural cilia, the design and fabrication of artificial cilia have attracted growing interest and are important for a wide range of applications, such as propelling microrobotics (Ye, Régnier & Sitti 2013; Lum *et al.* 2016; Liu *et al.* 2020; Hu, Zhang & Shelley 2022), and pumping and mixing fluid in fluidics. In artificial systems at microscales, the beating mechanism of natural cilia seems impractical to realize. To mimic the ciliary beating patterns and generate non-reciprocal motions, various external actuation mechanisms have been explored, including light (Van Oosten, Bastiaansen & Broer 2009), pneumatic (Milana *et al.* 2019), electric fields (den Toonder *et al.* 2008) and especially magnetic fields (Khaderi *et al.* 2009; Shields *et al.* 2010; Khaderi *et al.* 2011; Lum *et al.* 2016; Hanasoge *et al.* 2017; Meng *et al.* 2019; Dong *et al.* 2020; Gu *et al.* 2020).

Instead of applying distributed motor forces, De Canio, Lauga & Goldstein (2017) showed that a single tangential follower force acting on the tip of a clamped elastic filament in a viscous fluid can also induce buckling and spontaneous oscillations through a Hopf bifurcation. Using the same phenomenological model, Man & Kanso (2020) demonstrated that multiple active filaments can display different synchronization states through hydrodynamic interactions. Although this driving mechanism does not require an external time periodicity, it is considered theoretically and not as a practical fluid pumping mechanism since the follower force is required to always remain tangential to the filament tip. To efficiently pump fluid at low Re, non-reciprocal trajectories with large swept areas are needed (Osterman & Vilfan 2011), which may be achieved through the buckling of an elastic filament under compression.

In this work, we propose a fluid pumping mechanism that can both exploit the buckling instability and is also more practical experimentally. We consider a composite cilium consisting of an elastic filament and a spherical particle attached at the filament tip, moving in a three-dimensional Stokesian fluid. The filament base is clamped to a no-slip wall and tilted from the normal direction of the wall. An external time-periodic force always parallel to the wall acts on the particle. Similar to the follower force model, the component of the driving force tangential to the filament tip in our model can induce filament buckling. The oscillation of the cilium is sustained by the component normal to the filament tip.

The benefit of introducing a spherical particle is twofold. First, the particle may be charged or carry a magnetic moment, allowing easier experimental realizations of a driving force applied at the filament tip using electric or magnetic fields. Second, the drag force of a spherical particle scales linearly as the particle radius b, and the characteristic filament force upon the fluid scales approximately as $L/\ln(L/a)$ (Cox 1970), where L is the filament length and a is the filament radius. Therefore, it is possible that the flux generated by the particle is comparable to or larger than the flux due to the filament as long as $b/L \gtrsim 1/\ln(L/a)$, which is a small value for a slender filament. Previous studies on artificial cilia only focused on elastic filaments or films, the effect of an attached particle has not been considered.

We first model the composite cilium numerically using a slender body theory. We observe that the cilium generates a large net flux at large tilt angles, accompanied by a buckling instability. The flux generated by the particle is indeed larger than the flux generated by the filament. The trajectories that the particle traces out depend sensitively on the buckling direction of the filament. As the buckling direction reverses, the particle

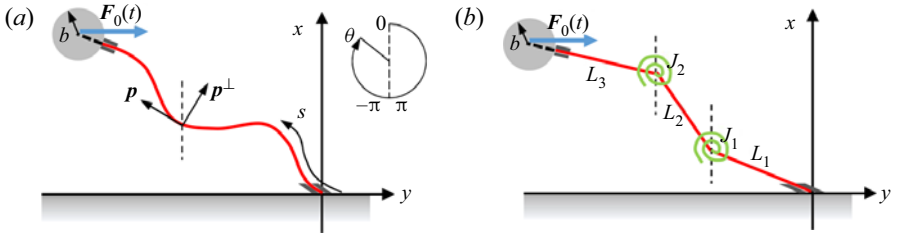

Figure 1. Schematic of a composite artificial cilium consisting of an elastic filament clamped at the base and a spherical particle attached at the filament tip. The cilium is driven by an external time-periodic force $\boldsymbol{F}_0(t)$ acting on the particle. (*a*) Elastic model, (*b*) segmental model.

trajectory and the generated net flux show abrupt changes. We also develop a reduced segmental model with a finite number of degrees of freedom that can reproduce similar dynamic behaviours. Finally, we discuss a possible experimental realization and estimate the magnitude of relevant parameters.

2. Model for an artificial cilium

We assume that the driving force acting on the particle is along the y direction with a simple sinusoidal form, $\boldsymbol{F}_0(t) = F_0(t)\hat{\boldsymbol{y}} = A\sin(2\pi t/\tau)\hat{\boldsymbol{y}}$, with A the amplitude and τ the period. We first model an elastic filament and then derive a segmental model using rigid segments.

2.1. *Dynamics of the composite cilium*

Consider a slender, inextensible and elastic filament (with the aspect ratio $\epsilon = a/L \ll 1$) and denote the filament position by $\boldsymbol{r}(s,t)$ with the arc length $s \in [-L/2, L/2]$. The unit tangent vector $\boldsymbol{p} = (\cos\theta, \sin\theta)$, with θ the tangent angle between $\boldsymbol{p}$ and $\hat{\boldsymbol{x}}$ (figure 1) and the unit normal vector $\boldsymbol{p}^\perp = (-\sin\theta, \cos\theta)$. The filament force per unit length is given by the Euler–Bernoulli elasticity $\boldsymbol{f} = -B\boldsymbol{r}_{ssss} + (T\boldsymbol{r}_s)_s$, where B is the bending rigidity and T is the filament tension. The filament force may be derived from the bending energy formulation with T acting as a Lagrange multiplier to enforce the filament inextensibility. From a non-local slender body theory (Johnson 1980), the velocity of the filament is given by

$$8\pi\mu(\boldsymbol{r}_t - \boldsymbol{U}_{p\to f}) = \Lambda[\boldsymbol{f}] + \mathcal{K}[\boldsymbol{f}], \tag{2.1}$$

where μ is the fluid viscosity and $\boldsymbol{U}_{p\to f}$ is the velocity generated by the particle at the filament. The local operator $\Lambda[\boldsymbol{f}] = [c(\boldsymbol{I} + \boldsymbol{r}_s\boldsymbol{r}_s) + 2(\boldsymbol{I} - \boldsymbol{r}_s\boldsymbol{r}_s)]\cdot\boldsymbol{f}$, where $c = |\ln(\epsilon^2 e)|$. The local operator captures the local drag anisotropy. From its inversion, we get the perpendicular and parallel anisotropic friction coefficients, $\xi_\perp = 8\pi\mu/(c+2)$ and $\xi_\parallel = 4\pi\mu/c$. In the limit of infinitely slender filaments one recovers the resistive force theory with $\xi_\perp/\xi_\parallel \approx 2$. The integral operator $\mathcal{K}[\boldsymbol{f}]$ captures the non-local interaction within the filament, which is interpreted as a disturbance velocity by the filament in the presence of a no-slip wall in our numerical computation. The filament velocity is then determined by a balance of viscous drag and the filament force $\boldsymbol{f}$. We write $8\pi\mu(\boldsymbol{r}_t - \boldsymbol{U}) = \Lambda[\boldsymbol{f}]$, where $\boldsymbol{U}$ includes $\boldsymbol{U}_{p\to f}$ and the contribution from the filament motion.

The filament tip is clamped to the particle surface, and the motion of the particle is fully determined by the translation and rotation of the filament at $s = L/2$. The particle position

$\boldsymbol{r}_p = (\boldsymbol{r} + b\boldsymbol{p})_{s=L/2}$ with b the particle radius, and its velocity $\boldsymbol{v}_p = (\boldsymbol{r}_t + b\theta_t \boldsymbol{p}^{\perp})_{s=L/2}$. We compute the disturbance velocity $\boldsymbol{U}$ as

$$\boldsymbol{U}(s) = \int_{-L/2}^{L/2} \boldsymbol{G}_\delta[\boldsymbol{r}(s), \boldsymbol{r}(s')] \cdot \boldsymbol{f}(s')\, \mathrm{d}s' + 6\pi\mu\chi b \boldsymbol{G}_\delta[\boldsymbol{r}(s), \boldsymbol{r}_p] \cdot \boldsymbol{v}_p. \tag{2.2}$$

Here, to account for the effect of the no-slip boundary, we use the regularized Blake tensor for a three-dimensional flow $\boldsymbol{G}_\delta$ with δ the regularization parameter (Blake 1971; Ainley *et al.* 2008); χ is a correction to the free-space Stokes drag (Happel & Brenner 2012), and χ increases as the particle approaches the no-slip boundary.

To ensure the filament inextensibility, we require $\boldsymbol{r}_s \cdot \boldsymbol{r}_{st} = 0$. Differentiating $\boldsymbol{r}_t$ with respect to the arc length and taking the tangent component, we obtain the tension equation

$$2cT_{ss} - (c+2)\theta_s^2 T = -8\pi\mu \boldsymbol{U}_s \cdot \boldsymbol{p} - 6cB\theta_{ss}^2 - (7c+2)B\theta_s\theta_{sss} + (c+2)B\theta_s^4. \tag{2.3}$$

The normal component of $\boldsymbol{r}_{st}$ gives the equation of θ, $\theta_t = \boldsymbol{r}_{st} \cdot \boldsymbol{p}^{\perp}$

$$8\pi\mu\theta_t + (c+2)B\theta_{ssss} = 8\pi\mu \boldsymbol{U}_s \cdot \boldsymbol{p}^{\perp} + (9c+6)B\theta_s^2\theta_{ss} + (3c+2)T_s\theta_s + (c+2)T\theta_{ss}. \tag{2.4}$$

We scale length on L, force on B/L^2 and time on the period of the driving force τ. The resulting elastoviscous number is $\eta = L/(B\tau/8\pi\mu)^{1/4}$, which compares the viscous force with the elastic force. The other two control parameters include the tilt angle θ_0 and the ratio of the particle radius to the filament length, $\beta = b/L$.

2.2. *Boundary conditions and numerical methods*

The orientation of the filament at $s = -L/2$ is fixed with $\theta = \theta_0$. The filament also has a zero velocity at $s = -L/2$, i.e. $\boldsymbol{r}_t = 0$. Separating the normal and tangent components of the filament velocity, this condition leads to $(T_s + 3B\theta_s\theta_{ss})_{s=-L/2} = 0$ and $(B\theta_{sss} - B\theta_s^3 - \theta_s T)_{s=-L/2} = 0$. The force and torque balance equations on the particle are

$$(-B\boldsymbol{r}_{sss} + T\boldsymbol{r}_s)_{s=L/2} = -6\pi\chi\mu b(\boldsymbol{v}_p - \boldsymbol{U}_{f\to p}) + \boldsymbol{F}_0(t), \tag{2.5}$$

$$(B\boldsymbol{r}_{ss} \times \boldsymbol{r}_s)_{s=L/2} = 8\pi\mu b^3 \omega_p \hat{\boldsymbol{z}}, \tag{2.6}$$

where $\boldsymbol{U}_{f\to p}$ is the velocity induced by the filament at the particle centre and captures the effect of filament motion on the particle motion, $8\pi\mu b^3$ is the rotational drag coefficient of a spherical particle and the particle angular velocity $\omega_p = (\theta_t)_{s=L/2}$. Since both $\boldsymbol{v}_p$ and ω_p are determined by the motion of the filament tip, (2.5) and (2.6) are translated into boundary conditions for θ and T. We solve (2.3) and (2.4) numerically using a second-order finite difference scheme (Tornberg & Shelley 2004). The coupled tension and θ equations with the nonlinear boundary conditions are solved using Newton's method. More details on the numerical methods can be found in Appendix A.

2.3. *Segmental model*

We replace an elastic filament with three rigid segments linked by torsional springs at the joints (figure 1*b*). The torsional spring exerts a torque proportional to the relative angle deflection between neighbouring segments. The total length of the segments is

fixed, $\sum_{j=1}^{3} L_j = L$, and the length ratios $\gamma_j = L_j/L$. The centreline of each segment $\boldsymbol{r}_j = \boldsymbol{r}_j^c + s_j\boldsymbol{p}_j$, where $\boldsymbol{r}_j^c$ is the centre-of-mass position and the unit tangent vector $\boldsymbol{p}_j = (\cos\theta_j, \sin\theta_j)$. We keep the clamped conditions by requiring that $\theta_1 = \theta_0$ and $\boldsymbol{p}_3$ passes through the particle centre. Integrating (2.1) for each segment along the arc length and ignoring the non-local interaction

$$8\pi\mu L_j\dot{\boldsymbol{r}}_j^c = [c(\boldsymbol{I} + \boldsymbol{p}_j\boldsymbol{p}_j) + 2(\boldsymbol{I} - \boldsymbol{p}_j\boldsymbol{p}_j)] \cdot \boldsymbol{F}_j, \tag{2.7}$$

where $\boldsymbol{F}_j$ is the total filament force upon the fluid. The torque-free condition of segment 3 with respect to J_2 is

$$K(\theta_2 - \theta_3)\hat{\boldsymbol{z}} + \boldsymbol{\sigma}_3^h|_{J_2} + (L_3 + b)\boldsymbol{p}_3 \times (-6\pi\chi\mu b\boldsymbol{v}_p + \boldsymbol{F}_0) = 0, \tag{2.8}$$

where K is the elastic modulus of the spring, the particle velocity $\boldsymbol{v}_p = \dot{\boldsymbol{r}}_3^c + (L_3/2 + b)\dot{\boldsymbol{p}}_3$ and the hydrodynamic torque acting on segment 3 about J_2 is computed as

$$\boldsymbol{\sigma}_3^h|_{J_2} = -\int_{-L_3/2}^{L_3/2} (s_3 + L_3/2)\boldsymbol{p}_3 \times \boldsymbol{f}_3 \,\mathrm{d}s_3. \tag{2.9}$$

The torque balance equation of segments 2 and 3 about joint J_1 is

$$\begin{aligned} &K(\theta_1 - \theta_2)\hat{\boldsymbol{z}} + \boldsymbol{\sigma}_2^h|_{J_1} + \boldsymbol{\sigma}_3^h|_{J_2} - L_2\boldsymbol{p}_2 \times \boldsymbol{F}_3 + [L_2\boldsymbol{p}_2 + (L_3 + b)\boldsymbol{p}_3] \\ &\quad \times (-6\pi\chi\mu b\boldsymbol{v}_p + \boldsymbol{F}_0) = 0, \end{aligned} \tag{2.10}$$

where $\boldsymbol{\sigma}_2^h|_{J_1}$ is the hydrodynamic torque acting on segment 2 about J_1, and the last term computes the torque of the driving force and the viscous drag of the particle. The system is closed by the constraints that the velocities of neighbouring segments at the joints are the same. We scale length on L, time on τ, force on K/L and torque on K. The resulting elastoviscous number $\eta = L/(K\tau/8\pi\mu)^{1/3}$. Hereafter, we use dimensionless variables with the same notation for both the elastic model and the segmental model.

3. Results

3.1. *Fluid pumping*

The motion of the artificial cilium reaches a steady state after a few periods. When $\theta_0 = 0$, the cilium beating patterns are periodic and symmetric over one period (figure 2*a*). The particle follows a symmetric 'figure-8' trajectory. As a result, the time-averaged disturbance flow field shows no net fluid pumping along the y direction (figure 2*b*). However, when $\theta_0 < 0$, we observe a distinct power ($F_0 < 0$) and recovery stroke ($F_0 > 0$). A typical example is shown in figure 2(*c*). The filament is stretched out during the power stroke (red). As $\boldsymbol{F}_0$ reverses, the filament is bent with large deformation and moves towards the $+y$ direction during the recovery stroke (blue). The particle traces out an asymmetric trajectory and the disturbance flow field shows a clear net flux along the $-y$ direction (figure 2*d*). The centre of mass of the filament also traces out an asymmetric trajectory, similar to the natural cilium (Brumley *et al.* 2014).

The pumping performance can be characterized by the flux of the disturbance flow field obtained by integrating the Blake tensor over the x–z plane perpendicular to the pumping direction (Liron 1978). The resulting instantaneous flux due to a point force of unit strength along the $+y$ direction located at a distance h from the no-slip wall is given by $h/\pi\mu$.

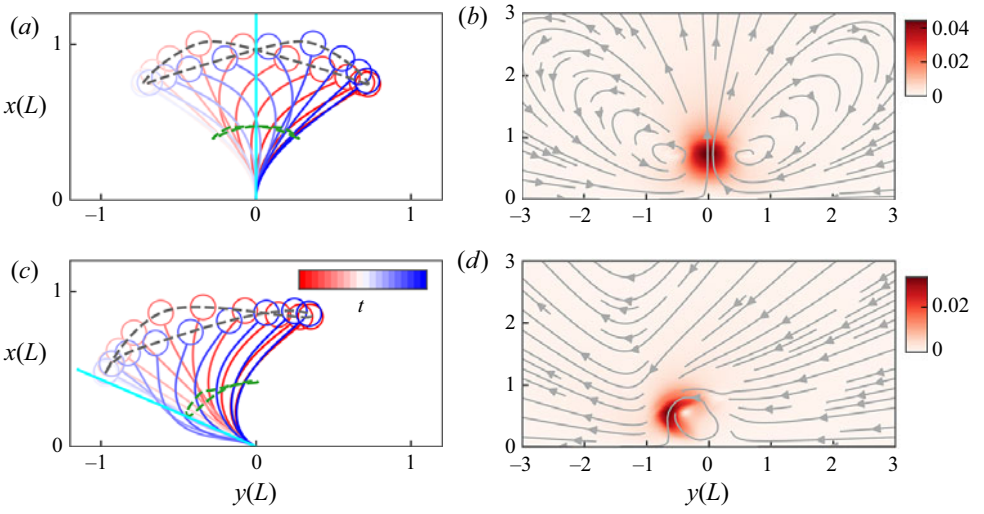

Figure 2. Time lapse of the artificial cilium over one forcing period in the steady state and the time-averaged disturbance flow field with $\eta = 3.5$ and $\beta = 0.08$ for (a,b) $\theta_0 = 0$ (see supplementary movie 1 available at https://doi.org/10.1017/jfm.2023.436), and (c,d) $\theta_0 = -1.16$ (supplementary movie 2). The force amplitude $A = 65$. Time runs from red to blue. The cyan lines in (a,c) indicate the initial orientations. The dark dashed lines show the particle trajectories and the green dashed lines show the centre-of-mass position of the filament. The colour bars in (c,d) show the magnitude of the flow speed and arrows indicate flow directions.

The net flux Q of the composite cilium consists of the flux generated by the filament Q_f and the flux generated by the particle Q_p

$$Q = Q_f + Q_p = \frac{1}{\pi\mu}\left\langle \int_{-L/2}^{L/2} x(s) f_y(s)\,\mathrm{d}s \right\rangle + 6b\langle \chi x_p \boldsymbol{v}_p \cdot \hat{\boldsymbol{y}} \rangle, \tag{3.1}$$

where $\langle\rangle$ denotes time average over a period in steady state and the distance of the particle from the wall $x_p = (x + b\cos\theta)|_{s=L/2}$. The particle flux $Q_p \approx 6b\langle x_p \boldsymbol{v}_p \cdot \hat{\boldsymbol{y}}\rangle = 6b\langle x_p \dot{y}_p\rangle = 6bS/\tau$, where S is the area swept by the particle (Osterman & Vilfan 2011). This states that Q_p is proportional to the area enclosed by the non-reciprocal trajectory of the particle.

Figure 3(*a*) shows the effect of θ_0 with fixed force amplitude $A = 65$. As $|\theta_0|$ increases (tilting towards the $-y$ direction), both $|Q_f|$ and $|Q_p|$ increase. Since the area swept by the particle is much larger than the area swept by the centre-of-mass position of the filament (figure 2*c*), $|Q_p|$ is always larger than $|Q_f|$. Surprisingly, for sufficiently large $|\theta_0|$, $|Q_f|$ and $|Q_p|$ drop abruptly to smaller values. The time lapse of the filament deformation shows that the abrupt change of Q_p is accompanied by a reversal of filament bending direction. As shown by the two insets in figure 3(*a*), the filament is bent downwards during the recovery stroke for $\theta_0 = -1.12$ and upwards for $\theta_0 = -0.96$. This difference in the filament deformation leads to a difference in the particle trajectories, and therefore an abrupt change in Q_p. A similar discontinuity is observed when varying the force amplitude A with fixed $\theta_0 = -0.9$ (figure 3*b*). As A is increased, the flux increases. When A becomes sufficiently large, both $|Q_f|$ and $|Q_p|$ jump to larger values with a reversal of the bending direction.

The filament bending direction is likely determined by deviation of cilium orientation at the start of the recovery stroke from the initial orientation, which is also the natural orientation at rest with no external force. We compute the deviation as

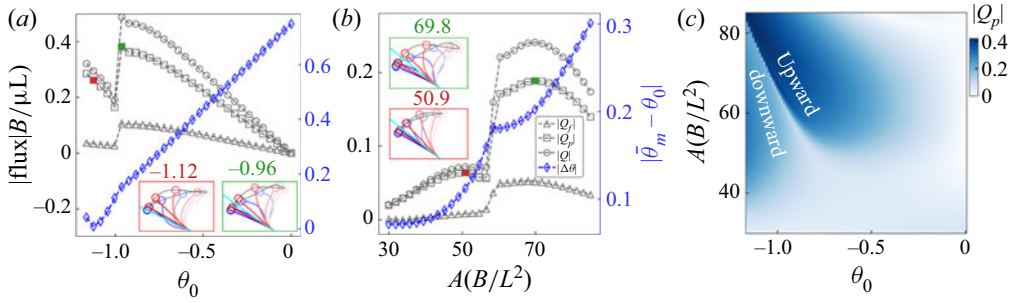

Figure 3. (*a*,*b*) Time-averaged flux $|Q_f|$ (left axis, dark triangles), $|Q_p|$ (left axis, dark squares) and the total flux $|Q|$ (left axis, dark circles) as a function of (*a*) the initial tilt angle θ_0 and (*b*) the force amplitude A with $\beta = 0.08$ and $\eta = 3.5$. The flux is scaled by $B/\mu L$. In (*a*) $A = 65$, and in (*b*) $\theta_0 = -0.9$. The deviations $|\Delta\theta| = |\bar{\theta}_m - \theta_0|$ are shown on the right axes by the blue diamonds. The insets show the time lapse of the artificial cilium for different values of (*a*) θ_0 (supplementary movies 3 and 4) and (*b*) A corresponding to the filled red and green squares. The initial orientations are marked by the cyan lines. Panel (*c*) shows $|Q_p|$ as a function of θ_0 and A.

$\Delta\theta = \bar{\theta}_m(t = n) - \theta_0$, where the average orientation in steady state $\bar{\theta}_m = \int_{-1/2}^{1/2} \theta(s)\,\mathrm{d}s$ and n is an integer. The deviation $|\Delta\theta|$ is largest for the symmetric case with $\theta_0 = 0$ (figure 2*a*). Figure 3(*a*,*b*) shows that $|\Delta\theta|$ decreases as the cilium is more tilted (with fixed A) or as the driving force A decreases (with fixed θ_0). The filament changes from downward bending to upward bending as $|\Delta\theta|$ exceeds a critical value around 0.15 in figure 3(*a*) and 0.18 in figure 3(*b*). As an example, the case of $\theta_0 = -1.12$ (downward bending) in figure 3(*a*) shows smaller deviation than the case of $\theta_0 = -0.96$ (upward bending). A similar observation can be made by comparing the two insets in figure 3(*b*) with $A = 50.9$ and $A = 69.8$.

We then compute the density plot of Q_p as functions of θ_0 and A. The values of A and θ_0 are limited to avoid the cilium touching the no-slip wall. As shown in figure 3(*c*), two regions with large negative flux are identified at large A and θ_0 corresponding to upward and downward bending. The sharp boundary separating these two regions spans a wide range for $\theta_0 \lessapprox -0.8$ and $A \gtrapprox 55$.

3.2. *Linear stability analysis*

When a filament is under compression at its tip along the tangential direction, the filament buckles as the compression exceeds a critical value (Landau & Lifshitz 1986). To investigate whether the tangent component of $\boldsymbol{F}_0$ is large enough to induce buckling in our system, especially at large values of $|\theta_0|$, we perform a linear stability analysis on the composite cilium with a tangential compression force Γ acting on the particle.

Consider a small deformation from an initially straight filament with $\theta_0 = 0$, then $x \sim s$, $\boldsymbol{p} \sim (1, y_x)$, and $\boldsymbol{p}^{\perp} \sim (-y_x, 1)$. We use non-dimensional equations and ignore the non-local interaction. The linearized tension equation is $T_{ss} = 0$ with $T_s = 0$ at $s = -1/2$ and $T + 3/2c\beta\chi T_s = -\Gamma$ at $s = 1/2$. This leads to $T = -\Gamma$. We linearize (2.1) as

$$-\alpha\Gamma y_{xx} - \alpha y_{xxxx} = y_t, \tag{3.2}$$

where $\alpha = \eta^{-4}(c + 2)$. The boundary conditions are

$$y = 0, \quad y_x = 0, \tag{3.3}$$

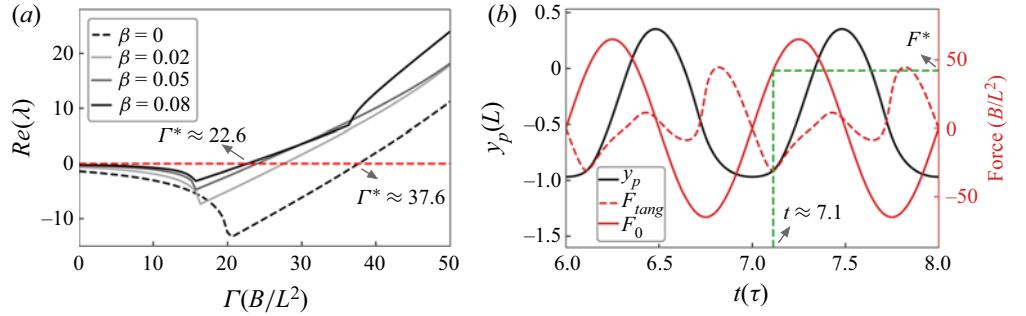

Figure 4. Linear stability analysis. (*a*) The real part of the largest eigenvalue $Re(\gamma)$ as a function of Γ for different values of β. (*b*) In steady state, the y-component position of the particle (dark curve, left axis), actuation force F_0 (red solid curve, right axis) and filament tangent force F_{tang} at $s = 1/2$ (red dashed curve, right axis) as a function of time with $A = 65$, $\eta = 3.5$, $\beta = 0.08$ and $\theta_0 = -1.12$. The green dashed lines indicate F_0^*, the value of F_0 at the maximum of $|F_{tang}|$ around $t \approx 7.1$.

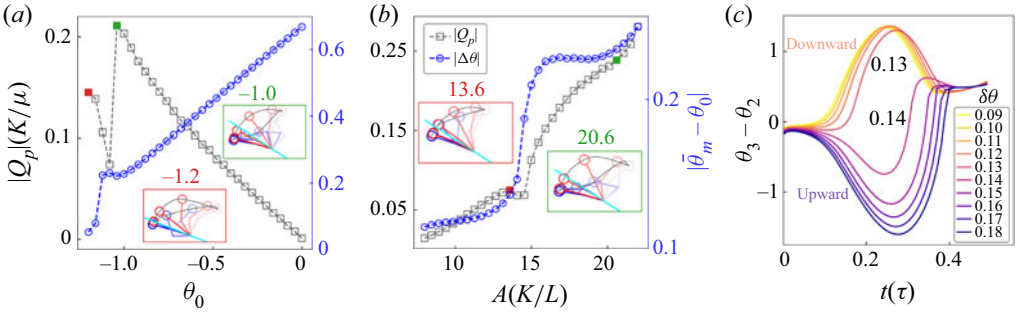

Figure 5. Results of the segmental model with $\beta = 0.08$, $\eta = 3.5$, and $\gamma_j = 1/3$. (*a*,*b*) The time-averaged flux generated by the particle $|Q_p|$ (dark squares, left axis) as a function of (*a*) θ_0 and (*b*) A. In (*a*) $A = 18.0$, and in (*b*) $\theta_0 = -1.0$. The flux is scale by K/μ. Insets show the time lapse of the artificial cilia for different values of (*a*) θ_0 (supplementary movies 5 and 6) and (*b*) A corresponding to the red and green squares. Cyan lines indicate initial orientations. The deviations $|\Delta\theta| = |\bar{\theta}_m - \theta_0|$ are shown on the right axes by the blue circles. (*c*) Relative deflection $\theta_3 - \theta_2$ under a constant driving force $F_0 = 18.0$ as a function of time t for different values of $\delta\theta$ with $\theta_0 = -1.0$.

at $s = -1/2$, and

$$y_{xx} + \beta^3\eta^4 y_{xt} = 0, \quad y_{xxx} - 3/4\eta^4\beta\chi(y_t + \beta y_{xt}) = 0, \tag{3.4a,b}$$

at $s = 1/2$. We consider perturbations of the form $y(x, t) = \phi(x)e^{\lambda t}$, and solve the resulting eigenvalue problem numerically using centred finite differences in the bulk and sided differences at the boundaries. Figure 4 shows that the real part of the largest eigenvalue $Re(\lambda)$ decreases first and then increases as Γ is increased. The system becomes unstable if $Re(\lambda) > 0$. For $\beta = 0$, the critical value $\Gamma^* \approx 37.6$, which agrees with the result given in De Canio *et al.* (2017). The critical value becomes smaller as β is increased. For $\beta = 0.08$, $\Gamma^* \approx 22.6$.

We observe a signature of buckling instability in our simulations. As shown in figure 5(*b*), computed with $\theta_0 = -1.12$ (corresponding to the left inset in figure 3*a*), although F_0 increases rapidly first during the recovery stroke starting at $t = 7.0$, the particle remains almost fixed for a period of time with little change in its y-component position. Meanwhile, the magnitude of the filament tangent force at $s = 1/2$, expressed as $F_{tang}|_{s=1/2} = [(-\boldsymbol{r}_{sss} + T\boldsymbol{r}_s) \cdot \boldsymbol{p}]_{s=1/2}$, increases and reaches a maximum at $t \approx 7.1$. The filament then buckles and the particle moves towards the $+y$ direction with F_{tang} released.

Therefore, we use $F^* = F_0(t \approx 7.1)$ to estimate the compression force acting on the composite cilia as $\Gamma = |F^* \sin(\theta_0)| \approx 37.9$. We apply the same approximation to the case of $\theta_0 = -0.96$ (the right inset in figure 3*a*) and obtain $\Gamma \approx 41.0$. Both estimates are larger than Γ^*, indicating that buckling instability indeed occurs at large $|\theta_0|$ and the abrupt change in the net flux is caused by a reversal of the filament buckling direction.

3.3. *Segmental model*

In the segmental model, the generated flux is also dominated by the contribution from the particle, especially at large $|\theta_0|$. Similar to the elastic model, abrupt change in Q_p is also observed when varying θ_0. Figure 5(*a*) shows that $|Q_p|$ first increases monotonically as $|\theta_0|$ increases from 0. For sufficiently large $|\theta_0|$, $|Q_p|$ suddenly jumps to a smaller value, along with a reversal of the buckling direction during the recovery stroke: segment 2 and segment 3 buckle upwards ($\theta_2 > \theta_3$, see inset with $\theta_0 = -1.0$) when $\theta_0 \gtrsim -1.0$ and downwards ($\theta_2 < \theta_3$, see inset with $\theta_0 = -1.2$) when $\theta_0 \lesssim -1.0$. An abrupt change in Q_p is also found when the force amplitude A is changed (figure 5*b*). As A exceeds a critical value around 22.5, segments 2 and 3 switch from a downward buckling to an upward buckling with a significant increase in $|Q_p|$. Comparing the two cases shown by the insets of figure 5(*b*) with $A = 13.6$ and 20.6, $|Q_p|$ is tripled with an apparent increase in the enclosed area by the particle trajectory. The average orientation of the cilium is $\bar{\theta}_m = (\theta_1 + \theta_2 + \theta_3)/3$, and the deviation from the natural orientation $\Delta\theta = \bar{\theta}_m - \theta_0$. The transition from downward buckling to upward buckling is accompanied with a pronounced increase in $|\Delta\theta|$.

Finally, to verify that the reversal of the buckling direction is indeed caused by the deviation from the natural orientation, we perform the following numerical experiment. We apply a constant driving force $F_0 = 18.0$ along the $+y$ direction and evolve the system for a time duration of 0.5. The deviation from a straight line is varied: we set $\theta_1(t = 0) = \theta_0$, $\theta_2(t = 0) = \theta_0 - \delta\theta$ and $\theta_3(t = 0) = \theta_0 - 2\delta\theta$, where $\delta\theta$ is the magnitude of the deviation. The buckling direction is characterized by the relative deflection between segments 2 and 3. As shown in figure 5(*c*), segments 2 and 3 buckle downwards with $\theta_3 - \theta_2 > 0$ for $\delta\theta \lessapprox 0.13$. An abrupt change occurs when $\delta\theta \gtrapprox 0.13$, segments 2 and 3 buckle upwards with $\theta_3 - \theta_2 < 0$ for most of the time and reach equilibrium positions as $t \to 0.5$.

4. Conclusions and discussion

In this work we have studied the dynamics of a spherical particle constrained by an elastic filament as a simple model of an artificial cilium at low *Re*. We constructed an elastic model using slender body theory and derived a reduced segmental model with linked rigid segments. We found that the particle trajectory is strongly non-reciprocal at large tilt angle due to the buckling of the filament and a net fluid pumping parallel to the no-slip wall is generated. The particle trajectory and the induced flux depend sensitively on the buckling direction of the filament. Using the segmental model, we demonstrated that as the deviation of the cilium orientation at the start of the recovery stroke from the natural orientation exceeds a threshold, a reversal of the buckling direction occurs, leading to abrupt changes in the particle trajectories and the net flux.

The composite cilium we proposed may be fabricated as a whole experimentally at millimetre scale or larger by moulding silicone elastomers (Hu *et al.* 2018; Lu *et al.* 2018; Gu *et al.* 2020), such as Ecoflex and Sylgard 184. Magnetic microparticles, like NdFeB, may be embedded within the spherical particle to provide a net moment after pre-magnetization. The cilium can then be driven by an external oscillating non-uniform

magnetic field. To check if the parameter ranges for the observed pumping behaviours are realistic, we perform order-of-magnitude estimates of relevant parameters. We assume the filament length $L = 2$ mm, the radius $a = 0.1$ mm and the particle radius $b = 0.2$ mm. The bending rigidity $B = \pi Y a^4/2 \sim 10^{-11}$ N m^2 for Ecoflex, where Y is the Young's modulus (Vaicekauskaite *et al.* 2020). Using numbers reported in previous experiments (Hu *et al.* 2018), the magnetization, which depends on the mass ratio of the magnetic particles and the magnitude of the magnetic field, may reach $M \sim 5 \times 10^5$ A m^{-1} for a field strength around 1 T. The resulting magnetic moment of the particle $m = 4\pi b^3 M/3 \sim 10^{-5}$ A m^2. To be comparable to the buckling threshold, $m\delta \sim 10B/L^2$, the field gradient $\delta \sim 1$ T/m, which is approximately one or two orders of magnitude smaller than the gradient around common rare-earth magnets and easily achievable.

The hydrodynamic interactions with the no-slip wall have a small effect on the overall pump performance but affect the transition points between the upward and downward buckling. We also performed limited simulations with different actuation profiles. Including a weak second harmonic generates a faster increase of the actuation force and a larger bending deformation of the filament during the recovery stroke, shifting the particle closer towards the wall. This leads to a larger swept area and improves the pump performance. For elastic filaments free to undergo three-dimensional motions, tangential compression along the filament can induce three-dimensional spinning (Ling *et al.* 2018). The filament in our model is confined to planar motion in the x–y plane and the stability against perturbations in the z direction is not analysed, but we speculate that the component of the driving force normal to the filament tip may favour motions in the x–y plane. We only considered a single cilium, and the results may be quite different in a cilium array due to hydrodynamic interactions. With a phase-dependent driving force, different synchronization states may arise by varying the ratio of particle radius to the filament length, leading to a different pump performance (Kotar *et al.* 2010, 2013; Chakrabarti & Saintillan 2019; Man & Kanso 2020; Chakrabarti *et al.* 2022; Kanale *et al.* 2022).

Supplementary movies. Supplementary movies are available at https://doi.org/10.1017/jfm.2023.436.

Acknowledgements. We thank J. Zhang for helpful comments and suggestions. We also thank the anonymous reviewers for their constructive comments and suggestions.

Funding. This work is supported by National Natural Science Foundation of China (grant nos 12275332, 12047503, and 12247130) and Chinese Academy of Sciences and Wenzhou Institute (grant no. WIUCASQD2023009). The computations of this work were conducted on the HPC cluster of ITP-CAS.

Declaration of interests. The authors report no conflict of interest.

Author ORCIDs.
Shiyuan Hu https://orcid.org/0000-0002-8415-4263;
Fanlong Meng https://orcid.org/0000-0002-8322-4696.

Appendix A. Numerical methods for the elastic model

We solve the elastic model using a second-order finite difference method. We discretize the arc length with a uniform grid of size Δs, $s_j = j\Delta s - 1/2$ with $j = 0, 1, \ldots, 1/\Delta s$, and denote the quantities at s_j with a subscript j. We discretize time as $t_n = n\Delta t$ and denote with a superscript n the quantities at the current time step t_n. Schematically, we write the non-dimensional θ equation (2.4) as

$$\frac{3\theta^{n+1} - 4\theta^n + \theta^{n-1}}{2\Delta t} + (\alpha\theta_{ssss} - 3\zeta\theta_s^2\theta_{ss} - \zeta T_s\theta_s - \alpha T\theta_{ss})^{n+1} = [\boldsymbol{U}_s \cdot \boldsymbol{p}^{\perp}]^n, \quad \text{(A1)}$$

where $\alpha = \eta^{-4}(c+2)$, $\zeta = \eta^{-4}(3c+2)$. Denoting the solutions at the kth Newton interaction with a superscript k, and linearizing (A1) around current guesses,

$$\delta\theta - \frac{2\Delta t\alpha}{3}\alpha\theta_{ss}^k\delta T + \frac{2\Delta t}{3}(-6\zeta\theta_s^k\theta_{ss}^k - \zeta T_s^k)\delta\theta_s + \frac{2\Delta t}{3}[-3\zeta(\theta_s^k)^2 - \alpha T^k]\delta\theta_{ss} + \frac{2\Delta t\alpha}{3}\delta\theta_{ssss} - \frac{2\Delta t\zeta}{3}\theta_s^k\delta T_s = \frac{4}{3}\theta^n - \frac{1}{3}\theta^{n-1} + \frac{2\Delta t}{3}[\boldsymbol{U}_s\cdot\boldsymbol{p}^{\perp}]^n + G[\theta^k, T^k], \quad \text{(A2)}$$

where $G[\theta^k, T^k]$ collects terms evaluated at iteration k. The tension equation (2.3) is linearized as

$$2c\delta T_{ss} - (c+2)(\theta_s^k)^2\delta T + [-2(c+2)\theta_s^k T^k + (7c+2)\theta_{sss}^k - 4(c+2)(\theta_s^k)^3]\delta\theta_s + 12c\theta_{ss}^k\delta\theta_{ss} + (7c+2)\theta_s^k\delta\theta_{sss} = -\eta^4[\boldsymbol{U}_s\cdot\boldsymbol{p}]^n + M[\theta^k, T^k], \quad \text{(A3)}$$

where $M[\theta^k, T^k]$ collects terms evaluated at iteration k. The boundary conditions are linearized in a similar way. Results from previous time steps are used as the initial guesses. Solving the resulting linear system for $\delta\theta$ and δT and iterating until converge, we obtain θ^{n+1} and T^{n+1}. For most of our simulations, $\Delta s = 10^{-2}$, $\Delta t = 5\times10^{-4}$, and the regularization parameter of the Blake tensor $\delta = 0.03$.

References

Ainley, J., Durkin, S., Embid, R., Boindala, P. & Cortez, R. 2008 The method of images for regularized stokeslets. *J. Comput. Phys.* **227** (9), 4600–4616.

Bayly, P.V. & Dutcher, S.K. 2016 Steady dynein forces induce flutter instability and propagating waves in mathematical models of flagella. *J. R. Soc. Interface* **13** (123), 20160523.

Blake, J.R. 1971 A note on the image system for a stokeslet in a no-slip boundary. *Proc. Camb. Phil. Soc.* **70**, 303.

Blake, J.R. & Sleigh, M.A. 1974 Mechanics of ciliary locomotion. *Biol. Rev.* **49** (1), 85–125.

Brumley, D.R., Wan, K.Y., Polin, M. & Goldstein, R.E. 2014 Flagellar synchronization through direct hydrodynamic interactions. *eLife* **3**, e02750.

Camalet, S., Jülicher, F. & Prost, J. 1999 Self-organized beating and swimming of internally driven filaments. *Phys. Rev. Lett.* **82** (7), 1590.

Chakrabarti, B., Fürthauer, S. & Shelley, M.J. 2022 A multiscale biophysical model gives quantized metachronal waves in a lattice of beating cilia. *Proc. Natl Acad. Sci. USA* **119** (4), e2113539119.

Chakrabarti, B. & Saintillan, D. 2019 Hydrodynamic synchronization of spontaneously beating filaments. *Phys. Rev. Lett.* **123** (20), 208101.

Cox, R.G. 1970 The motion of long slender bodies in a viscous fluid. Part 1. General theory. *J. Fluid Mech.* **44** (4), 791–810.

De Canio, G., Lauga, E. & Goldstein, R.E. 2017 Spontaneous oscillations of elastic filaments induced by molecular motors. *J. R. Soc. Interface* **14** (136), 20170491.

Dong, X., Lum, G.Z., Hu, W., Zhang, R., Ren, Z., Onck, P.R. & Sitti, M. 2020 Bioinspired cilia arrays with programmable nonreciprocal motion and metachronal coordination. *Sci. Adv.* **6** (45), eabc9323.

Faubel, R., Westendorf, C., Bodenschatz, E. & Eichele, G. 2016 Cilia-based flow network in the brain ventricles. *Science* **353** (6295), 176–178.

Gu, H., *et al*. 2020 Magnetic cilia carpets with programmable metachronal waves. *Nat. Commun.* **11** (1), 1–10.

Hanasoge, S., Ballard, M., Hesketh, P.J. & Alexeev, A. 2017 Asymmetric motion of magnetically actuated artificial cilia. *Lab on a Chip* **17** (18), 3138–3145.

Happel, J. & Brenner, H. 2012 *Low Reynolds Number Hydrodynamics: With Special Applications to Particulate Media*, vol. 1. Springer Science & Business Media.

Hu, W., Lum, G.Z., Mastrangeli, M. & Sitti, M. 2018 Small-scale soft-bodied robot with multimodal locomotion. *Nature* **554** (7690), 81–85.

Hu, S., Zhang, J. & Shelley, M.J. 2022 Enhanced clamshell swimming with asymmetric beating at low Reynolds number. *Soft Matt.* **18** (18), 3605–3612.

Johnson, R.E. 1980 An improved slender-body theory for stokes flow. *J. Fluid Mech.* **99** (2), 411–431.

JUAN, R.-S., GUILLERMINA, R., MATHIJSSEN, A.J.T.M., HE, M., JAN, L., MARSHALL, W. & PRAKASH, M. 2020 Multi-scale spatial heterogeneity enhances particle clearance in airway ciliary arrays. *Nat. Phys.* **16** (9), 958–964.

KANALE, A.V., LING, F., GUO, H., FÜRTHAUER, S. & KANSO, E. 2022 Spontaneous phase coordination and fluid pumping in model ciliary carpets. *Proc. Natl Acad. Sci. USA* **119** (45), e2214413119.

KHADERI, S.N., BALTUSSEN, M.G.H.M., ANDERSON, P.D., IOAN, D., DEN TOONDER, J.M.J. & ONCK, P.R. 2009 Nature-inspired microfluidic propulsion using magnetic actuation. *Phys. Rev.* E **79** (4), 046304.

KHADERI, S.N., CRAUS, C.B., HUSSONG, J., SCHORR, N., BELARDI, J., WESTERWEEL, J., PRUCKER, O., RÜHE, J., DEN TOONDER, J.M.J. & ONCK, P.R. 2011 Magnetically-actuated artificial cilia for microfluidic propulsion. *Lab on a Chip* **11** (12), 2002–2010.

KOTAR, J., DEBONO, L., BRUOT, N., BOX, S., PHILLIPS, D., SIMPSON, S., HANNA, S. & CICUTA, P. 2013 Optimal hydrodynamic synchronization of colloidal rotors. *Phys. Rev. Lett.* **111** (22), 228103.

KOTAR, J., LEONI, M., BASSETTI, B., LAGOMARSINO, M.C. & CICUTA, P. 2010 Hydrodynamic synchronization of colloidal oscillators. *Proc. Natl Acad. Sci. USA* **107** (17), 7669–7673.

LANDAU, L.D. & LIFSHITZ, E.M. 1986 *Theory of Elasticity*, vol. 7. Elsevier.

LAUGA, E. & POWERS, T.R. 2009 The hydrodynamics of swimming microorganisms. *Rep. Prog. Phys.* **72** (9), 096601.

LING, F., GUO, H. & KANSO, E. 2018 Instability-driven oscillations of elastic microfilaments. *J. R. Soc. Interface* **15** (149), 20180594.

LIRON, N. 1978 Fluid transport by cilia between parallel plates. *J. Fluid Mech.* **86** (4), 705–726.

LIU, Z., QIN, F., ZHU, L., YANG, R. & LUO, X. 2020 Effects of the intrinsic curvature of elastic filaments on the propulsion of a flagellated microrobot. *Phys. Fluids* **32** (4), 041902.

LU, H., ZHANG, M., YANG, Y., HUANG, Q., FUKUDA, T., WANG, Z. & SHEN, Y. 2018 A bioinspired multilegged soft millirobot that functions in both dry and wet conditions. *Nat. Commun.* **9** (1), 3944.

LUM, G.Z., YE, Z., DONG, X., MARVI, H., ERIN, O., HU, W. & SITTI, M. 2016 Shape-programmable magnetic soft matter. *Proc. Natl Acad. Sci. USA* **113** (41), E6007–E6015.

MAN, Y. & KANSO, E. 2020 Multisynchrony in active microfilaments. *Phys. Rev. Lett.* **125** (14), 148101.

MENG, F., BENNETT, R.R., UCHIDA, N. & GOLESTANIAN, R. 2021 Conditions for metachronal coordination in arrays of model cilia. *Proc. Natl Acad. Sci. USA* **118** (32), e2102828118.

MENG, F., MATSUNAGA, D., YEOMANS, J.M. & GOLESTANIAN, R. 2019 Magnetically-actuated artificial cilium: a simple theoretical model. *Soft Matt.* **15**, 3864–3871.

MILANA, E., GORISSEN, B., PEERLINCK, S., DE VOLDER, M. & REYNAERTS, D. 2019 Artificial soft cilia with asymmetric beating patterns for biomimetic low-Reynolds-number fluid propulsion. *Adv. Funct. Mater.* **29** (22), 1900462.

ORIOLA, D., GADÊLHA, H. & CASADEMUNT, J. 2017 Nonlinear amplitude dynamics in flagellar beating. *R. Soc. Open Sci.* **4** (3), 160698.

OSTERMAN, N. & VILFAN, A. 2011 Finding the ciliary beating pattern with optimal efficiency. *Proc. Natl Acad. Sci. USA* **108** (38), 15727–15732.

PURCELL, E.M. 1977 Life at low Reynolds number. *Am. J. Phys.* **45** (1), 3–11.

SHIELDS, A.R., FISER, B.L., EVANS, B.A., FALVO, M.R., WASHBURN, S. & SUPERFINE, R. 2010 Biomimetic cilia arrays generate simultaneous pumping and mixing regimes. *Proc. Natl Acad. Sci. USA* **107** (36), 15670–15675.

DEN TOONDER, J., *et al*. 2008 Artificial cilia for active micro-fluidic mixing. *Lab on a Chip* **8** (4), 533–541.

TORNBERG, A.-K. & SHELLEY, M.J. 2004 Simulating the dynamics and interactions of flexible fibers in stokes flows. *J. Comput. Phys.* **196** (1), 8–40.

VAICEKAUSKAITE, J., MAZUREK, P., VUDAYAGIRI, S. & SKOV, A.L. 2020 Mapping the mechanical and electrical properties of commercial silicone elastomer formulations for stretchable transducers. *J. Mater. Chem.* C **8** (4), 1273–1279.

VAN OOSTEN, C.L., BASTIAANSEN, C.W.M. & BROER, D.J. 2009 Printed artificial cilia from liquid–crystal network actuators modularly driven by light. *Nat. Mater.* **8** (8), 677–682.

YE, Z., RÉGNIER, S. & SITTI, M. 2013 Rotating magnetic miniature swimming robots with multiple flexible flagella. *IEEE Trans. Robot.* **30** (1), 3–13.